## PAPER

Check for updates

# Charge storage kinetics of interconnected MnO$_2$ nano-needles/reduced graphene oxide composite for high energy density quasi-solid-state sodium ion asymmetric supercapacitor†

Deependra Jhankal,[a] Mohammad Saquib Khan,[b] Preeti Shakya,[b] Nikita Bhardwaj,[a] Bhanu Yadav,[a] K. K. Jhankal[c] and K. Sachdev ⬤ *[ab]

In this study, a facile synthesis route for preparing manganese dioxide (MnO$_2$) with unique nano-needle morphology and its nanocomposite with reduced graphene oxide (MnO$_2$–rGO) for high energy density quasi-solid-state asymmetric supercapacitor (ASC) application is reported. Morphological characterizations indicate that the MnO$_2$ nano-needles are uniformly decorated on rGO sheets, creating an interconnected structure with rGO. The MnO$_2$–rGO nanocomposite shows good pseudocapacitive electrochemical behavior in a potential domain from 0 to 1.0 V. The detailed analysis of the cyclic voltammetry (CV) profiles of the rGO and MnO$_2$–rGO electrodes indicate that their sodium ion storage kinetics are based on ideal capacitive-controlled and pseudocapacitive (capacitive and diffusive) controlled processes, respectively. Furthermore, a quasi-solid-state ASC device is constructed by employing the MnO$_2$–rGO nanocomposite and rGO as the positive and negative electrodes, respectively. The fabricated ASC (rGO‖MnO$_2$–rGO) device operates within the wide cell potential range from 0 to 1.8 V and possesses the highest capacitance of 216 F g$^{-1}$, at the current density of 1 A g$^{-1}$, which is superior to that of the recently reported literatures. The ASC (rGO‖MnO$_2$–rGO) device displays an energy density of 24.25 W h kg$^{-1}$ at corresponding power density of 900 W kg$^{-1}$ along with significant cycle stability over the 6000 cycles. Thus, the morphological design of an advanced electrode material to boost the capacitance and potential window with the polymer gel electrolyte will aid in the fabrication of high energy density storage devices.

## 1. Introduction

In the last decade, the global energy demand has increased exponentially due to the fast growth in the human population. Traditional energy resources (*e.g.*, fossil fuels) are the key energy sources, but these are limited and largely contribute to global warming.[1–3] In this regard, using renewable energy sources to stop the alarming global climate change is the primary research concern for scientific society. Energy storage technologies with high energy densities are essential to the long-term growth of renewable energy sources. Nowadays, supercapacitors (SCs) have great potential in advanced and sustainable storage devices because of their high energy

density, long cyclability, fast charging–discharging processes, ultrahigh value of capacitance, flexibility, cost-effective, ease of fabrication, and eco-friendly nature.[4–7]

Asymmetric supercapacitors (ASCs) are primarily utilized for the high energy density ($E = 1/2CV^2$) energy storage devices by tuning the operating potential window of the device. The ASC contains two different types of electrodes, where one electrode (negative electrode) has an electric double layer capacitance (EDLC) and the other electrode (positive electrode) has the pseudocapacitive type of charge storage mechanism.[8] Modern improved graphene-related materials are frequently utilized as negative electrode materials for ASCs because of their superior physiochemical features and greater surface area.[9–11] Various pseudocapacitive metal oxides, such as V$_2$O$_5$, Co$_3$O$_4$, RuO$_2$, and Fe$_3$O$_4$ have been widely employed as positive electrode materials for ASCs owing to their numerous valence states and higher theoretical specific capacitance.[12–15] In comparison to other materials, MnO$_2$ is a promising metal oxide for a high-performance pseudocapacitive material due to several outstanding features, such as its cost-effectiveness, abundant

[a] *Department of Physics, Malaviya National Institute of Technology, Jaipur 302017, India. E-mail: ksachdev.phy@mnit.ac.in*

[b] *Materials Research Centre, Malaviya National Institute of Technology, Jaipur 302017, India*

[c] *Department of Chemistry, University of Rajasthan, Jaipur 302004, India*

† Electronic supplementary information (ESI) available. See DOI: https://doi.org/10.1039/d3ya00469d

availability, high specific capacitance, low molecular weight, wide potential window in an aqueous electrolyte, and environmental friendliness.[16–18] In the charge storage processes, the fast-reversible redox-reaction ($MnO_2 \leftrightarrow MnOOC$, C = $H^+$, $K^+$, $Na^+$, $Li^+$) has occurred on the surface of $MnO_2$, which enhances the capacitance.[19,20] However, $MnO_2$ still suffers from inferior electrochemical properties due to its lower electrical conductivity in the domain of $10^{-5}$ to $10^{-6}$ S cm$^{-1}$ and limited cycle stability, which restrict its further practical applications.[21,22]

To overcome the abovementioned issues, several approaches have been adopted, such as the incorporation of $MnO_2$ with polymers, graphene, and carbon nanotubes (CNTs), to enrich the electrochemical activity of $MnO_2$.[23–28] Among these approaches, the formation of the $MnO_2$ nanocomposite with sp$^2$ hybridized two-dimensional reduced graphene oxide (rGO) has received a lot of attention for SCs. In the nanocomposite, rGO not only acts as the high conductive support for $MnO_2$, but also improves the rate performance by facilitating the fast charge transportation in the nanocomposite.[29–31] Additionally, the morphologically modified nanostructure of $MnO_2$ can cover a large surface area with the electrolyte, which can explore all available active sites, leading to enhancement of capacitance.

ASCs with wide potential windows have recently adopted various prospective strategies to boost the capacitive performance of $MnO_2$. For instance, Gomaa prepared $MnO_2$ nanoflowers as the positive electrode material for ASC in $Na_2SO_4$ electrolyte containing a maximum capacitance of 177.6 F g$^{-1}$ at a current density of 0.25 A g$^{-1}$.[32] Liangshuo et al.[33] used porous carbon and the $MnO_2$ nanowire/porous carbon composite as negative and positive electrodes, respectively, for efficient ASC. The performance of the ASC device was enhanced due to the large surface area of the $MnO_2$ nanowires, which facilitate the additional diffusion paths for feasible ions with the electrolyte. Geerthana et al.[34] reported on rGO (negative electrode) and α-$Fe_2O_3$/$MnO_2$/rGO (positive electrode) with PVA/KOH as the gel-electrolyte for an advanced ASC that contained a maximum energy density of 13.2 W h kg$^{-1}$. Thus, to the best of our knowledge, the fabrication of $MnO_2$ with a unique nano-needle morphology and its uniform distribution on rGO sheets as the positive electrode for sodium ion-based quasi-solid-state ASC has not been reported elsewhere.

Herein, we proposed a hydrothermal method for the synthesis of $MnO_2$ with unique nano-needle morphology. Additionally, we synthesized rGO as the conducting support for $MnO_2$ and as the negative electrode material for the ASC device by hydrothermal route. To enhance the electrochemical performance of $MnO_2$, we synthesized the $MnO_2$ nano-needle interconnected with rGO sheets ($MnO_2$–rGO nanocomposite) by hydrothermal strategy. Additionally, the separator-less electrolyte, PVA/$Na_2SO_4$, was used to create the ASC device using $MnO_2$–rGO and rGO as the positive and negative electrodes, respectively. The fabricated ASC (rGO‖$MnO_2$–rGO) device was operated in a wide potential window (0–1.8 V), and exhibited the highest energy density of 24.5 W h kg$^{-1}$ with significant cyclic stability.

# 2. Materials and methods

## 2.1. Materials

The following materials were provided by Alfa Aesar: acetylene black (>99%), sodium hydroxide (NaOH), hydrochloric acid (HCl – 35%), hydrogen peroxide ($H_2O_2$ – 30%), and graphite powder 325 mesh. Sodium nitrate ($NaNO_3$ – 99%) and sulphuric acid (95–97%) were acquired from Fisher Scientific. From LOBA Chemicals, we purchased potassium permanganate ($KMnO_4$ – 99%), isopropyl alcohol (IPA), and carboxymethyl cellulose (CMC, High pure).

## 2.2. Synthesis of $MnO_2$ nano-needles

$MnO_2$ with unique nano-needle morphology was synthesized by hydrothermal method. Briefly, 60 mL of deionized (DI) water was used to dissolve 1 g of $KMnO_4$, and the mixture was subsequently stirred continuously for 30 minutes. Then, 10 mL of HCl was added dropwise into the previous $KMnO_4$ solution under stirring in order to obtain a homogenous solution. Then, the reaction mixture was heated for 16 hours at 140 °C in a Teflon-lined autoclave. After the reaction was finished, the brown colored precipitate was separated, washed and dried at 60 °C overnight. The obtained $MnO_2$ nano-needles were annealed in a muffle furnace for three hours at 400 °C.[35]

## 2.3. Preparation of the $MnO_2$–rGO nanocomposite

The hydrothermal technique was adopted for the preparation of the nanocomposite. To create a homogeneous solution, 70 mL of DI water was used to disperse 70 mg of $MnO_2$ and 30 mg of rGO (the synthesis technique for GO and rGO is provided in the ESI†). Afterwards, the reaction mixture was poured into a Teflon-based autoclave, and heated in a hot air oven to 160 °C for 16 h. After the cooling down of the autoclave, a solid residue was then washed and dried at 60 °C overnight in a vacuum oven. Fig. S2 (ESI†) illustrates the synthesis strategy of $MnO_2$ and the $MnO_2$–rGO nanocomposite.

## 2.4. Electrode preparation

In this study, a glassy carbon electrode (GCE) modified through electrochemical ink made from synthesized electrode materials was utilized as the working electrode. The electrochemical ink was formed by dissolving the active material (e.g., rGO, $MnO_2$ and $MnO_2$–rGO nanocomposite), acetylene black and CMC in IPA solution (8 : 1 : 1). The electrochemical results were recorded in 1 M $Na_2SO_4$ electrolyte.

## 2.5. Assembly of the asymmetric supercapacitor device

For the fabrication of the ASC device, the stainless steel (SS) foil (2 cm × 2 cm) was utilized as a current collector. The SS foil was covered with the electrochemical ink of rGO and $MnO_2$–rGO using the drop-casting method, and the electrodes were heated at 120 °C for 12 hours. For the quasi-solid-state ASC device, a hydrogel membrane made of PVA and $Na_2SO_4$ was employed as the separator-less electrolyte. The mass loading ratio between the cathode (positive electrode) and anode (negative electrode) was calculated using charge balance eqn (S12) (in ESI†).

# 3. Results and discussions

## 3.1. FE-SEM analysis

Fig. 1(a) illustrates the FE-SEM picture of the as-synthesized $MnO_2$, indicating the nano-needle morphology of $MnO_2$. The diameter variation of the nano-needles is shown by the particle size distribution histogram (Fig. 1(b)), which shows the diameter of these nano-needles varying from 52 nm to 65 nm. The FE-SEM images of the $MnO_2$–rGO nanocomposite are depicted in Fig. 1(d and e), demonstrating that the $MnO_2$ nano-needles are uniformly decorated on the rGO sheets, forming an interconnected heterostructure with the rGO sheets. The morphology enhances the electrochemical performance by preventing the restacking of graphene sheets and providing fast ion transport during electrochemical processes. Fig. 1(c and f) show the elemental mapping of the $MnO_2$–rGO nanocomposite, which demonstrates that the sample has three major elements (Mn, O, and C) that are homogeneously dispersed.

## 3.2. Raman analysis

Fig. 2(a) displays the results of the Raman spectroscopic study of the synthesized rGO, $MnO_2$, and $MnO_2$–rGO composite. The Raman spectrum of rGO exhibits two distinctive peaks, the D band and G band, which appear at $\sim 1352$ $cm^{-1}$ and $\sim 1584$ $cm^{-1}$, respectively. The D band emerges owing to the disorder and defects present in the graphene sample, while the G band appears due to the vibration of the C=C/C–C bonded carbon atoms.[36] The Raman spectra of pure $MnO_2$ has two prominent peaks at $\sim 568.3$ $cm^{-1}$ and $\sim 630.6$ $cm^{-1}$, corresponding to the stretching vibration of the Mn–O and $MnO_6$ octahedral group of $MnO_2$, respectively.[37,38] The Raman spectrum of the $MnO_2$–rGO nanocomposite possesses both D and G bands, along with two prominent peaks of $MnO_2$, which suggests the presence of both $MnO_2$ nano-needles and rGO sheets. The slightly high value of $I_D/I_G$ for $MnO_2$–rGO (1.02), as compared to rGO (0.98), indicates an increase in defects on the



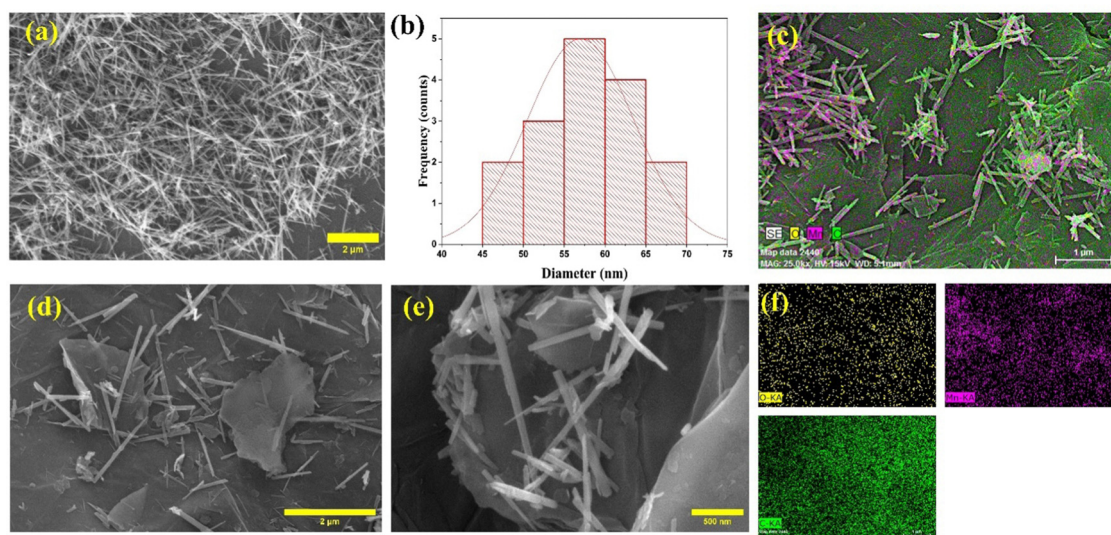Fig. 1 (a) SEM image of the $MnO_2$ nano-needles, (b) $MnO_2$ nano-needles diameter size distribution, (d)–(e) FE-SEM image of the $MnO_2$–rGO nanocomposite, and (c) and (f) $MnO_2$–rGO nanocomposite elemental mapping.



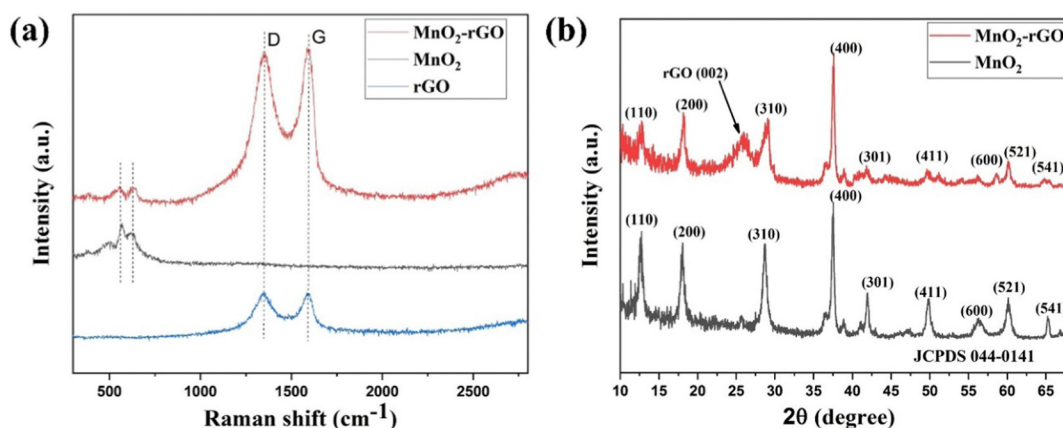Fig. 2 (a) Raman spectrum of rGO, pure $MnO_2$ and $MnO_2$–rGO, (b) XRD pattern of pure $MnO_2$ and $MnO_2$–rGO.

rGO sheets in MnO$_2$–rGO by coupling of the MnO$_2$ nano-needles. The morphology of the nano-composite ensures congruence between the MnO$_2$ nano-needles and rGO sheets, boosting the nanocomposite's electrochemical capabilities.[39,40]

### 3.3.  XRD study

The XRD study of MnO$_2$ and MnO$_2$–rGO were performed to analyze the crystal structure, phase and purity, which are illustrated in Fig. 2(b). The XRD spectra of pure MnO$_2$ shows major peaks at $2\theta$ = 12.7°, 18.1°, 28.8°, 36.6°, 37.52°, 41.96°, 49.86°, 56.37°, 60.27°, 69.71°, and 78.59°, corresponding to the (110), (200), (310), (400), (211), (301), (411), (600), (521), (542) and (332) crystal planes of α-MnO$_2$.[41] The position and intensity of all diffraction peaks coincide with JCPDS card No. 044-0141 with a tetragonal structure and the space group of 1 4/$m$. No extra peaks appear in the XRD pattern of MnO$_2$, indicating that the sample is in a pure phase without any impurities. Fig. S3 (ESI†) indicates the XRD pattern of rGO, which shows a broad peak at 24.6° that corresponds to the (002) plane.[42] The XRD pattern of MnO$_2$–rGO shows a broad peak at $2\theta$ = 24.6° corresponding to the rGO (002) plane, along with all prominent peaks of MnO$_2$.[43] The sharp peaks of both MnO$_2$ and the MnO$_2$–rGO nanocomposite suggest the good crystalline nature of the synthesized samples. Additionally, the crystallite size $D$ (nm) of the synthesized samples was evaluated by Scherrer's equation:

$$D = \frac{K\lambda}{\beta \cos \theta} \tag{1}$$

Here, $\lambda$, $K$, $\beta$ and $\theta$ symbolize the wavelength of the X-ray source (1.54 Å for Cu K$_\alpha$), Scherrer's constant (0.9), FWHM

(radian) of the peak and peak position, respectively.[44] The observed average crystallite size of the pure MnO$_2$ and MnO$_2$–rGO nanocomposite are 22.37 nm and 19.24 nm, respectively. In the case of the MnO$_2$–rGO nanocomposite, the reduced average crystallite size can further improve the performance of the nanocomposite.

### 3.4.  XPS analysis

In the survey spectra of rGO (Fig. 3(a)), only two peaks are observed, corresponding to C 1s and O 1s without having any other impurity elemental peaks. The high-resolution C 1s spectra (Fig. 3(b)) contain four major peaks that arise at 284.5, 285.1, 286.1 and 288.3 eV and correspond to C–C/C=C, C–O, C=O and O–C=O, respectively.[45,46] Additionally, the XPS analysis of MnO$_2$ was performed to observed its surface element compositions. The wide range survey spectra of MnO$_2$ (Fig. 3(a)) illustrate the existence of the intense peaks of O 1s and Mn 2p without any impurity elemental peaks. The deconvolution spectra of Mn 2p (Fig. 3(c)) display the two sub-peaks occurring at 641.5 and 653.2 eV that correspond to Mn 2p$_{3/2}$ and Mn 2p$_{1/2}$, respectively, indicating the +4 oxidation state of Mn. The full range survey spectra of the MnO$_2$–rGO nanocomposite (Fig. 3(a)) shows that MnO$_2$–rGO exhibits the major peaks of C 1s, O 1s, and Mn 2p with the corresponding binding energies of 286 eV, 532 eV, and 650 eV, respectively. Fig. 3(d) illustrates the deconvolution XPS spectrum of C 1s, which acquires three major peaks at 284.8 eV, 285.5 eV and 287.6 eV. The peak at 284.7 eV is ascribed to C–C/C=C, whereas the peaks at 285.5 eV and 287.6 eV are attributed to the hydroxyl (C–O) and carbonyl (C=O) groups, respectively.[47,48] Fig. 2(e) depicts the high-resolution XPS Mn 2p spectrum, which exhibits two sub-components at 641.9 eV and 653.6 eV that are ascribed to the Mn
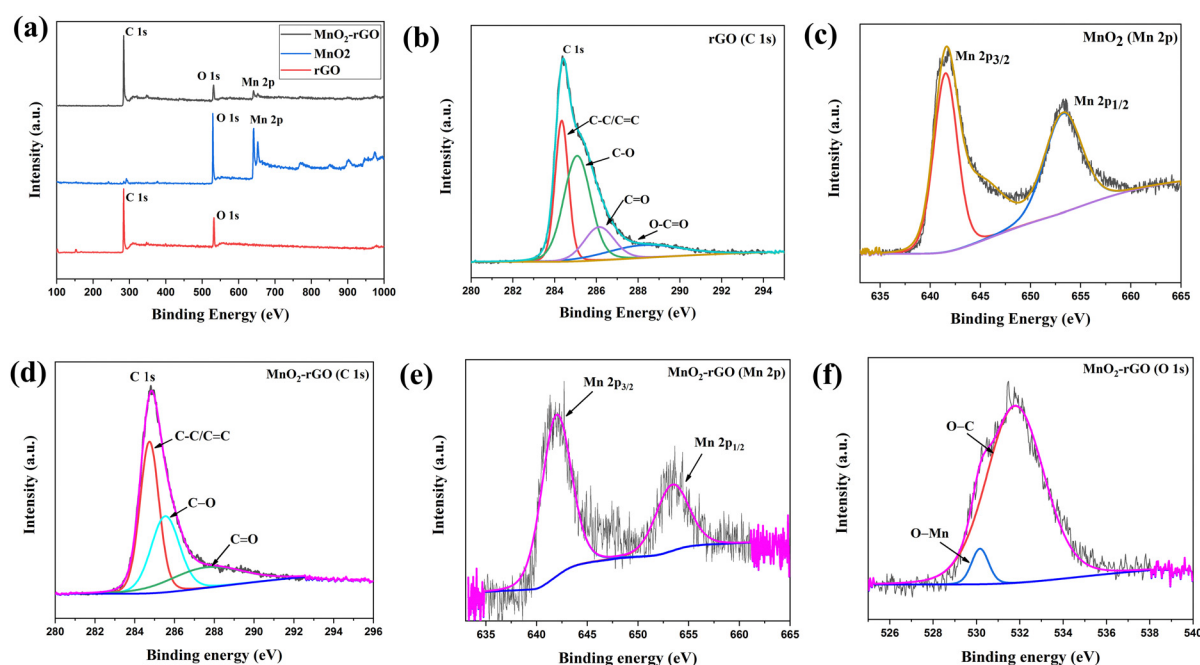


**Fig. 3** (a) Full scan survey spectra of rGO, MnO$_2$ and the MnO$_2$–rGO nanocomposite. The deconvoluted XPS spectrum of (b) rGO (C 1s) and (c) MnO$_2$ (Mn 2p). High-resolution XPS spectrum of (d) C 1s, (e) Mn 2p, and (f) O 1s of the MnO$_2$–rGO nanocomposite.

$2p_{3/2}$ and Mn $2p_{1/2}$ states of $MnO_2$, respectively.[48] It should be noted that the peak difference between Mn $2p_{3/2}$ and Mn $2p_{1/2}$ for both $MnO_2$ and $MnO_2$–rGO is approximately the same (11.7 eV), which demonstrates that $MnO_2$ maintains its stoichiometry during the formation of the composite with rGO. These components are assigned to the +4 oxidation state of $MnO_2$. Furthermore, the core level O 1s spectra of the $MnO_2$–rGO nanocomposite (Fig. 3(f)) shows two peaks: one peak at 531 eV that is ascribed to O bonded with manganese (Mn–O) in $MnO_2$, and the other one at 532 eV is assigned to the O–C band of graphene.[49]

### 3.5. TEM analysis of the $MnO_2$–rGO nanocomposite

The surface morphology, interlayer distance, and *d*-spacing of the $MnO_2$–rGO nanocomposite were examined using the TEM, HR-TEM, and selected area diffraction (SAD) pattern. Fig. 4(a) shows the TEM images of $MnO_2$–rGO at various resolutions where uniformly distributed $MnO_2$ nano-needles are seen on the rGO sheets, making an interconnected heterostructure, which would facilitate the fast ion/electron transport during charging/discharging. Fig. 4(b and c) displays the HR-TEM images of the $MnO_2$–rGO nanocomposite, which shows the layered lattice fringes of $MnO_2$ with an interlayer spacing of 0.55 nm. The SAED pattern of the $MnO_2$–rGO nanocomposite is depicted in Fig. 4(d), which shows the diffraction spots corresponding to the (110), (200), (310) and (400) crystal planes of tetragonal α-$MnO_2$, suggesting the good crystallinity of the $MnO_2$ nano-needle morphology in the $MnO_2$–rGO nanocomposite.

### 3.6. BET Analysis of the $MnO_2$–rGO nanocomposite

As an effective surface area is a crucial characteristic for the electrode material, the multipoint surface area and pore size distribution of the $MnO_2$–rGO nanocomposite was governed by $N_2$ adsorption/desorption isotherms technique (BET Analysis), as depicted in Fig. 4(e) and Fig. 4(f), respectively. The shape of Fig. 4(e) suggests the mesoporous structure of the $MnO_2$–rGO nanocomposite.[50] The mesoporosity arises due to the interconnected $MnO_2$ nano-needles with interspersed rGO sheets, providing a unique and advantageous morphology to the sample. The specific surface area of the $MnO_2$–rGO nanocomposite was obtained as 49.92 m$^2$ g$^{-1}$. The average pore size and pore volume in the $MnO_2$–rGO nanocomposite was measured to be 1.52 nm and 0.147 cm$^3$ g$^{-1}$, respectively. The appropriate multipoint surface area and mesoporous structure of the $MnO_2$–rGO nanocomposite play a vital role in efficient ions/electrons transport, and also facilitate the large number of diffusion channels for massive charge storage during electrochemical processes, therefore enhancing the overall electrochemical performance of the nanocomposite.

## 4. Electrochemical characterizations

### 4.1. Electrochemical study of rGO electrode (negative electrode)

The CV profiles for the rGO-electrode were recorded in 1 M aqueous $Na_2SO_4$ electrolyte within the potential range of −0.8 V to 0 V at various sweep rates (10 mV s$^{-1}$ to 100 mV s$^{-1}$), and are depicted in Fig. 5(a). The CV curves show an almost rectangular shape, revealing the ideal capacitive nature of rGO. The CV curves maintain their shape at higher scan rates, without exhibiting any signal deformation, demonstrating the electrode material's superior electrochemical reversibility and stability.[51] Additionally, a comprehensive analysis of the CV profile was carried out to observe the charge-storage mechanisms in the rGO-electrode utilizing the power law:[52,53]
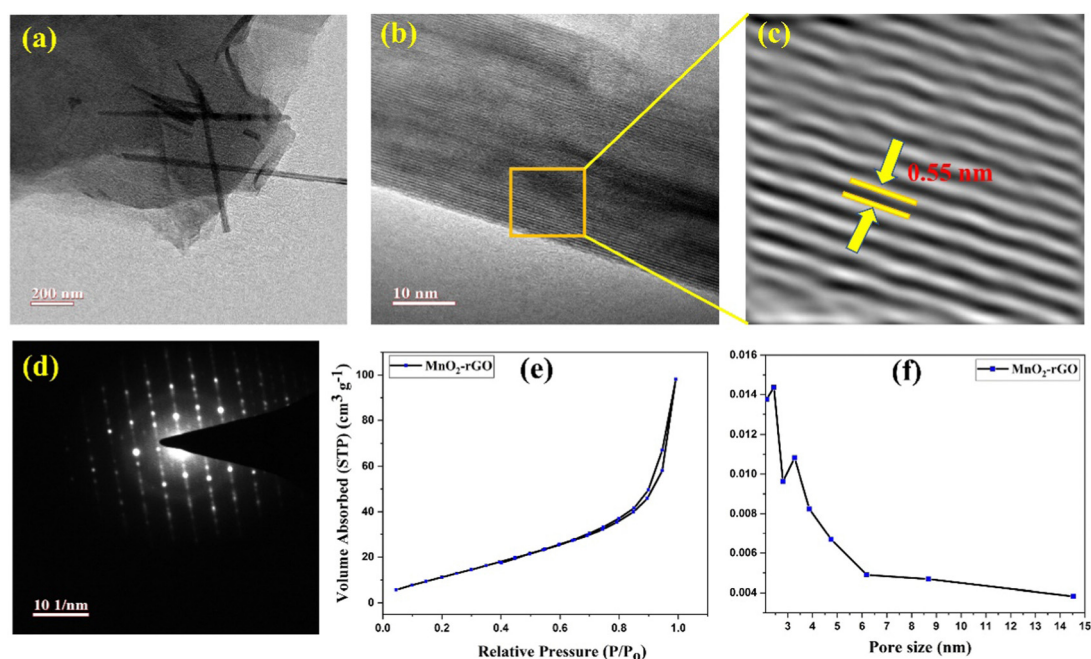


Fig. 4 (a) TEM images, (b) and (c) HR-TEM pictures and (d) SAED pattern of the $MnO_2$–rGO nanocomposite. (e) BET curve and (f) pore size distribution curve of the $MnO_2$–rGO nanocomposite.
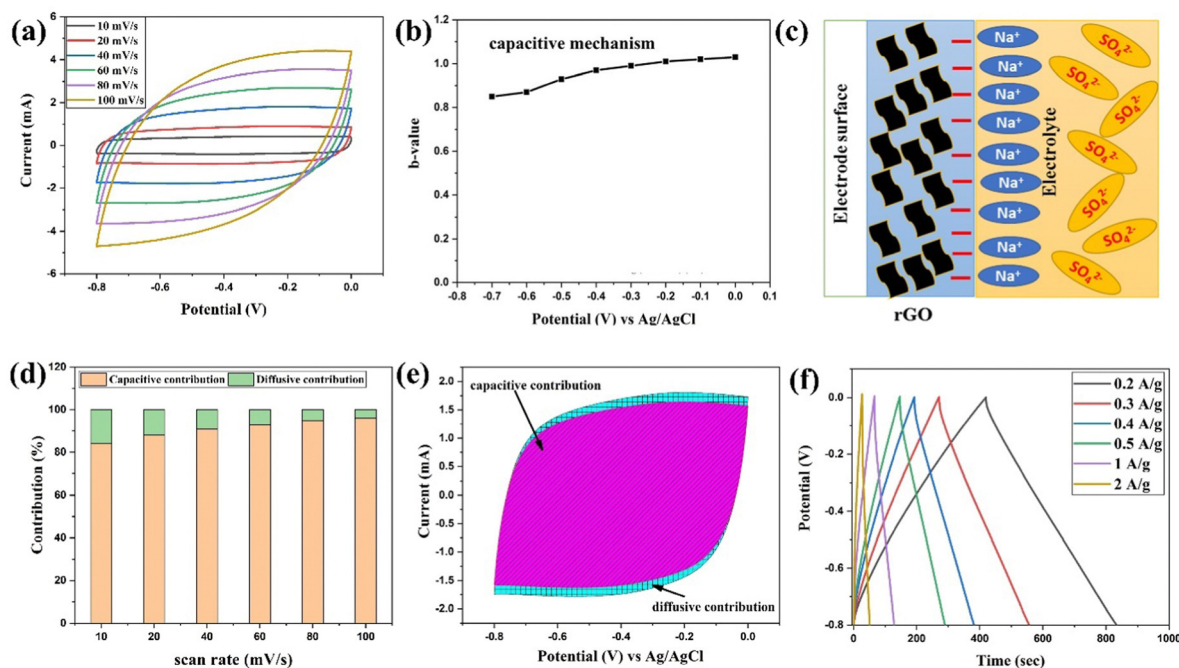
Fig. 5 (a) CV profile of the rGO-electrode at several sweep rates. (b) Variation of the *b* value at various applied voltages. (c) Graphical illustration of the charge storage in the rGO electrode. (d) Percentage capacitive and diffusive contribution as the function of scan rates of the rGO-electrode. (e) CV curve of the rGO electrode (at 40 mV s⁻¹) and (f) GCD curve for the rGO electrode at different current densities.

$$i = av^b \tag{2}$$

$$\log i = b \log v + \log a \tag{3}$$

here, *i* represents the total current, *v* refers to the sweep rate, while *a* and *b* denote the constants. The slope of the linear fit curve between $\log i$ *vs.* $\log v$ provide the value of *b*, and this *b* value describes the type of charge storage kinetics of the electrode, such as non-faradaic capacitive processes ($b = 1$), diffusion-controlled battery type processes ($b = 0.5$) and pseudocapacitive processes (fast redox reactions on surface, $0 < b < 1$).[54] Fig. S4(a) (in ESI†) shows the linear fit curve between $\log i$ *vs.* $\log v$ for the rGO electrode at different applied voltages. The obtained *b* values at different voltages are shown in Fig. 5(b), which are found to vary between 1 to 1.15, suggesting the pure capacitive type of nature of the rGO-electrode by creation of the double layer of charge on the electrode and electrolyte interface, as depicted in Fig. 5(c).

Furthermore, the storage process of electrodes was determined by Dunn's method, specified by the below equation:[55]

$$i\,(V) = a_1 v + a_2 v^{1/2} \tag{4}$$

Here, $a_1 v$ denotes the non-diffusive limited process, while $a_2 v^{1/2}$ signifies the diffusive controlled kinetics process. For ease of calculation, re-design the above equation to:

$$\frac{i\,(V)}{v^{1/2}} = a_1 v^{1/2} + a_2 \tag{5}$$

A curve of $i\,(V)/v^{1/2}$ *vs.* $v^{1/2}$ gives the value of $a_1$ (slope) and $a_2$ (intercept). Fig. S4(c) (ESI†) shows the linear fit plot between $v^{1/2}$ *vs.* $i\,(V)/v^{1/2}$ for the rGO-electrode at different applied

voltages. The variation of percentage contribution of each process (non-diffusive and diffusive limited) along with several scan rates are mentioned in Fig. 5(d), which shows that the contribution of the non-diffusive process has a progressively growing tendency, indicating the capacitive-controlled nature of the rGO-electrode. The dominating nature of the non-faradaic capacitive process of the rGO-electrode is favorable for the long-term device cyclic stability.[53] The rGO-electrode possesses 94% contribution of the non-faradaic limited process, as depicted in Fig. 5(e). This suggests the dominance of the capacitive-controlled kinetics of the electrode, which makes the rGO-electrode as the negative electrode for the ASC device. In an ASC device, the general electrode reaction at the graphene-based negative electrode during charging/discharging can be described as follows:[56]

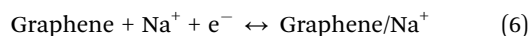$$Graphene + Na^+ + e^- \leftrightarrow Graphene/Na^+ \tag{6}$$

Fig. 5(f) illustrates the GCD profiles of the rGO electrode, which shows a nearly triangular shape, again indicating the capacitive behavior of the electrode. From eqn (S2) (ESI†), the obtained values of the specific capacitance ($C_{sp}$) are 105.5 F g⁻¹, 108.75 F g⁻¹, 96.5 F g⁻¹, 90.6 F g⁻¹, 82.5 F g⁻¹ and 65 F g⁻¹ at a current density of 0.2 A g⁻¹, 0.3 A g⁻¹, 0.4 A g⁻¹, 0.5 A g⁻¹, 1 A g⁻¹ and 2 A g⁻¹, respectively.

### 4.2. Electrochemical study of MnO₂–rGO-electrode (positive electrode)

The CV profiles of MnO₂ and the MnO₂–rGO-electrode were recorded at 100 mV s⁻¹ in the potential range 0 to 1 V, and are depicted in Fig. S5 (ESI†). The CV profiles show the

MnO$_2$–rGO-electrode possessing a high loop area, indicating a high value of capacitance as compared to the MnO$_2$-electrode. The high capacitance of the MnO$_2$–rGO-electrode could be attributed to the synergistic effect in the MnO$_2$–rGO nanocomposite caused by the significant pseudocapacitive contribution of MnO$_2$ and the high electronic conductivity of the rGO sheets.[25] The quasi-rectangular CV curves of the MnO$_2$–rGO-electrode at several sweep rates are depicted in Fig. 6(a), proposing the pseudocapacitive nature of the charge storage of the MnO$_2$–rGO-electrode. The CV curve maintains its shape at all sweep rates, which reveals the improved stability of the electrode material.[51] The interconnected structure of the MnO$_2$/rGO nanocomposite could facilitate numerous diffusion channels for fast faradaic reactions. Furthermore, the interconnected structure can reduce the diffusion length of the electrolyte ions, which provide a faster permeation of ions to the porous MnO$_2$/rGO composite electrode material, resulting in a high value of capacitance and stability of the electrode even at a higher scan rate.[57]

The $b$ value in the applied potential domain of 0 V to 1 V was evaluated from the linear fit curve between $\log i$ $vs.$ $\log \upsilon$ of the MnO$_2$–rGO-electrode at different applied voltages, which is depicted in Fig. S4(b) (in ESI†). The obtained $b$ values (Fig. 6(b)) are found to be in the range of 1.2 to 0.95 at lower potential (0.1 V to 0.3 V), indicating the charge storage at lower potentials to be largely due to the capacitive processes. Conversely, the $b$ values of 0.55 to 0.45 occur at higher potentials ($>$0.3 V), suggesting the charge storage mechanism of the MnO$_2$–rGO-electrode (Fig. 6(c)) to be predominantly diffusion-

controlled for potentials greater than 0.3 V. The faradaic diffusive mechanism is more dominating in the MnO$_2$–rGO-electrode due to the presence of MnO$_2$ nano-needles on the surface of the rGO sheets, which provide a hetero-interface to the intercalation/de-intercalation of the electrolyte ions. Fig. S4(d) (ESI†) shows the linear fit plot between $\upsilon^{1/2}$ $vs.$ $i$ (V)/$\upsilon^{1/2}$ for the MnO$_2$–rGO electrode at different applied voltages. Fig. 6(d) represents the variation of the percentage contribution of the non-diffusive (capacitive) and diffusion-limited processes along with several scan rates, which indicates that the dominance of the diffusion-controlled contribution of the total current response of the MnO$_2$–rGO electrode. Fig. 6(e) depicts the CV curve of the MnO$_2$–rGO-electrode at a scan rate of 40 mV s$^{-1}$, indicating that 88% of the total current response is because of the diffusive-controlled kinetics. This reveals the dominance of the faradaic diffusive kinetics of electrode, resulting in a superior positive electrode for ASC application. The charge storage kinetics of MnO$_2$ in the Na$_2$SO$_4$ aqueous electrolyte, which include both intercalation/de-intercalation processes and adsorption/desorption, are described by the following equations:[58,59]

$$(\text{MnO}_2)_{\text{surface}} + \text{Na}^+ + \text{e}^- \leftrightarrow (\text{MnO}_2{}^n\text{–Na}^+)_{\text{surface}} \quad (7)$$

$$\text{MnO}_2 + \text{Na}^+ + \text{e}^- \leftrightarrow \text{MnOONa} \quad (8)$$

Fig. 6(f) displays the GCD measurements in 1 M Na$_2$SO$_4$ electrolyte of the MnO$_2$–rGO-electrode at different applied current densities. The GCD curves are not exactly triangular in shape, which shows that the electrode has pseudocapacitive charge storage characteristics. The calculated values of $C_{\text{sp}}$
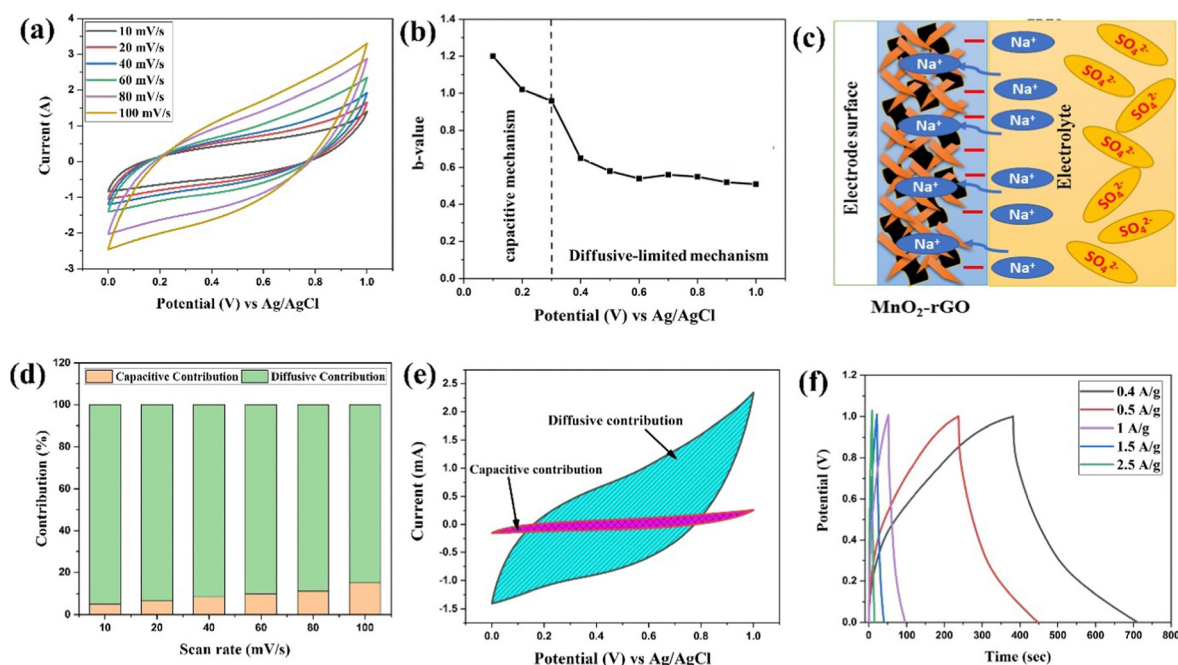


Fig. 6 (a) CV curves of the MnO$_2$–rGO electrode at the different sweep rates. (b) Variation of the b value at various applied voltages for the MnO$_2$–rGO electrode. (c) Graphical illustration of the charge storage in the MnO$_2$–rGO electrode. (d) Percentage of the capacitive and diffusive contributions of the MnO$_2$–rGO-electrode at different scan rates. (e) CV curve of the MnO$_2$–rGO-electrode (at 40 mV s$^{-1}$) and (f) GCD curve for the MnO$_2$–rGO electrode at several current densities.

(using eqn (S2), ESI†) are 132.8 F g$^{-1}$, 108.5 F g$^{-1}$, 53 F g$^{-1}$, 31.5 and 22.5 F g$^{-1}$ at a current density of 0.4 A g$^{-1}$, 0.5 A g$^{-1}$, 1 A g$^{-1}$, 1.5 A g$^{-1}$ and 2 A g$^{-1}$, respectively. It can be observed that even at a high current density, the MnO$_2$–rGO-electrode maintains a high value of capacitance. This suggests the good reversibility of the MnO$_2$–rGO-electrode, which could arise due to the combined effect of the MnO$_2$–rGO nanocomposite where the MnO$_2$ nano-needles interconnected structure (with the rGO sheets) facilitates the highly interconnected diffusive channels for fast transportation of the electrolyte ions/electrons.[60,61]

### 4.3. EIS study of rGO, MnO$_2$ and MnO$_2$–rGO-electrodes

EIS spectroscopy was employed to assess the electrodes' charge transfer resistance and interfacial kinetics. The EIS Nyquist plots of rGO, MnO$_2$ and the MnO$_2$–rGO-electrodes in the frequency domain of 1 MHz to 1 mHz are depicted in Fig. 7(a). The Nyquist plots of all three electrodes have mainly two regimes; that is, the high frequency semicircle and well-known low frequency linear Warburg zone. The equivalent circuit of the EIS study (Fig. 7(b)) was drawn for a better understanding of the electrode behavior, which involved primarily four elements: series resistance ($R_s$), charge transfer resistance ($R_{ct}$), and two constant phase elements (CPEs) (because to the distribution of uniform responses on the porous electrode surface, CPE is being considered in place of an ideal capacitor). CPE1 is created by the adsorption of ions, which results in the development of an electric double layer capacitance (EDLC), whereas CPE2 is created by the transport of electrolyte ions between the electrode and electrolyte interface, which results in the creation of pseudocapacitance.[62] The intercept of a semicircle on the real axis provides the value of

$R_s$, while the width of the semicircle is known as the faradaic charge transfer resistance ($R_{ct}$).[63] The observed values of $R_s$ and $R_{ct}$ for rGO, MnO$_2$ and the MnO$_2$–rGO electrode are mentioned in Table S1 (ESI†). The lowest value of $R_{ct}$ for the MnO$_2$–rGO-electrode (12.14 Ω) is due to the synergistic effect of both MnO$_2$ and rGO, which provide the fast electron transfer during charging/discharging, and boost the capacitive effectiveness of the electrode. Additionally, the complex power was analyzed from the EIS spectra to evaluate the operational response time of the fabricated electrodes. The complex power ($|S|$) of an electrochemical system is described by-

$$|S(\omega)| = |P(\omega) + jQ(\omega)| \tag{9}$$

Here, $P(\omega)$ and $Q(\omega)$ represent the real part and imaginary part of the complex power, respectively. The $P(\omega)$ and $Q(\omega)$ are also known as active and reactive power, respectively.

$$|P(\omega)| = \omega C''(\omega)|E_{rms}|^2 \tag{10}$$

$$|Q(\omega)| = \omega C'(\omega)|E_{rms}|^2 \tag{11}$$

Here, $C''$ and $C'$ are known as the imaginary and real parts of the capacitance, which are further defined by –

$$C'' = \frac{Z'}{\omega|Z|^2} \tag{12}$$

$$C' = \frac{-z''}{\omega|z|^2} \tag{13}$$

Fig. 7(c and d) shows the change in active power ($|P|/|S|$) and reactive power ($|Q|/|S|$) along with frequency for rGO, MnO$_2$, and the MnO$_2$–rGO electrodes. The active power ($|P|/|S|$) is
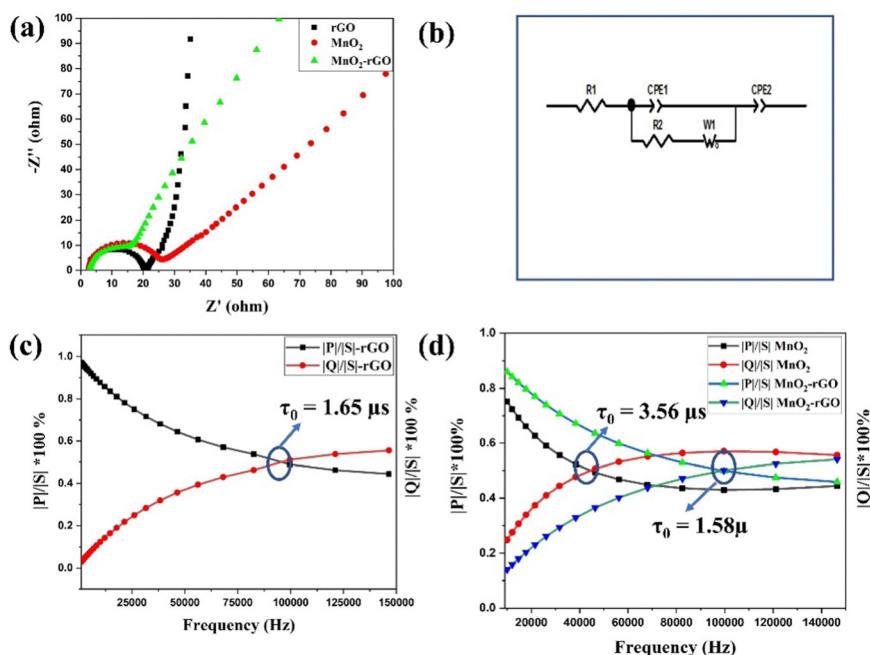


Fig. 7  (a) EIS spectra of rGO, MnO$_2$ and the MnO$_2$–rGO electrode, (b) equivalent fitted circuit of the EIS data. Plot between $|P|/|S|$ and $|Q|/|S|$ along with frequency (Hz) for the (c) rGO-electrode and (d) MnO$_2$ and MnO$_2$–rGO-electrode.

mainly contributed by power dissipated at high frequency, whereas the reactive power ($|Q|/|S|$) is primarily contributed by power dissipated at high frequency, and the supercapacitor acts as pure resistor and pure capacitor in the first and second conditions, respectively. The operational response time ($\tau_0$) is a crucial parameter for a supercapacitor, which describes the minimum time in which a supercapacitor changes its state from resistive behavior to capacitive behavior.[64] The $\tau_0$ is determined by the following equation:

$$\tau_0 = \frac{1}{2\pi f_0} \tag{14}$$

Here, $f_0$ represents the characteristic frequency, which is obtained from the intersect frequency point of the $|P|/|S|$ and $|Q|/|S|$ curves. The calculated values of $\tau_0$ for the rGO, MnO$_2$ and MnO$_2$–rGO-electrodes are 1.65 μs, 3.5 μs and 1.58 μs, respectively. The smaller value of $\tau_0$ for the MnO$_2$–rGO-electrode as compared to that of MnO$_2$ shows the benefit of the composite for the superior electrochemical performance of the supercapacitor. To further illustrate the charge storage kinetics, the Bode-phase diagrams (variation of the phase angle ($\Phi$) with respect to frequency) of rGO, MnO$_2$ and MnO$_2$–rGO-electrode were constructed, as shown in Fig. S6 (ESI†). The value of $\Phi$ defines the different rate-limiting kinetics, such as $\Phi = 0°$ for ideal resistive behavior, whereas $\Phi = -90°$ and $\Phi = -45°$ correspond to the ideal capacitive and diffusive-controlled processes, respectively. The observed value of $\Phi$ for the rGO electrode is $-82°$ (close to capacitive behavior) at low frequency (10 mHz), which shows the ideal capacitive nature of the rGO-electrode. It can be observed that $\Phi = -35°$ for MnO$_2$ and $\Phi = -65°$ for the MnO$_2$–rGO-electrode, which shows the nearly diffusive-controlled and pseudocapacitive (capacitive and diffusive) behavior of these materials, respectively.[65] The pseudocapacitive nature

of the MnO$_2$–rGO-electrode is attributed to the synergistic effect of the interconnected structure of the MnO$_2$–rGO nanocomposite, where MnO$_2$ and rGO contribute to the diffusive and capacitive capacitance, resulting in enhanced electrochemical performance of the electrode.

### 4.4. Electrochemical performance of fabricated ASC (rGO‖MnO$_2$–rGO) device

For practical utilization, the fabricated ASC (rGO‖MnO$_2$–rGO) device (Fig. 8(a)) was investigated by CV, GCD and EIS techniques. The mass ratio ($m_+/m_-$) was determined using the charge balance equation (eqn (S8), ESI†) to assemble the ASC device, and it was found to be 0.57. Fig. 8(b) shows the CV curves of the rGO and MnO$_2$–rGO-electrodes at 40 mV s$^{-1}$, which show that the rGO and MnO$_2$–rGO-electrodes operated in negative (0 to $-0.8$ V) and positive (0 to 1 V) potential windows, respectively, for better performances (as discussed above). So, the ASC (rGO‖MnO$_2$–rGO) device was designed to operate in the potential range of 0 to 1.8 V for superior performance. The CV curves of the ASC (rGO‖MnO$_2$–rGO) device for different cell potential windows at 100 mV s$^{-1}$ are depicted in Fig. 8(c). It is seen that the CV curves maintain the shape at every potential window without any significant distortion, indicating good voltage stability of the device. Fig. 8(d) shows the CV profile of the ASC (rGO‖MnO$_2$–rGO) device at increasing scan rates from 10 to 400 mV s$^{-1}$ in the wide cell potential window of 0 to 1.8 V. Even at higher scan rates, the CV voltammograms of the ASC device preserve their shape without any signal distortion, indicating the device's good cyclic stability and reversibility.

The specific capacitance ($C_{sp}$) values of the fabricated ASC (rGO‖MnO$_2$–rGO) device at different current densities are obtained from the GCD profiles, shown in Fig. 8(e). The GCD curves are observed to have a substantially symmetric triangular
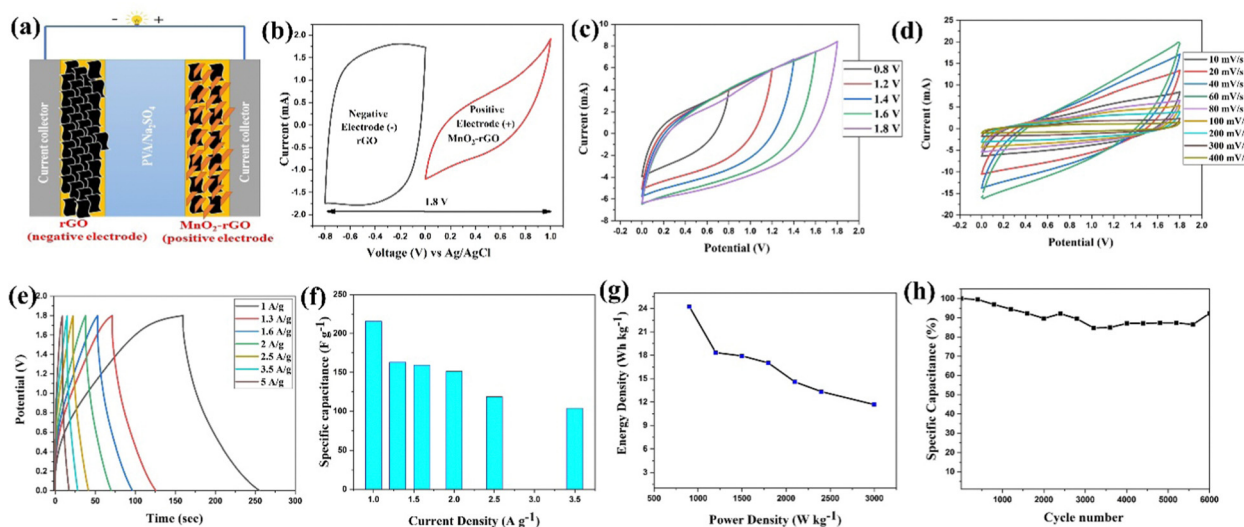


**Fig. 8** (a) Schematic representation of the fabricated asymmetric SC device. (b) CV curve of the individual rGO and MnO$_2$–rGO electrode at 40 mV s$^{-1}$ scan rate. (c) CV profile of the fabricated ASC device at several cell potentials. (d) CV profile of the fabricated ASC device at different scan rates. (e) GCD curves of the fabricated ASC (rGO‖MnO$_2$–rGO) device at different current densities. (f) Calculated capacitance at several applied current densities. (g) Ragone plot for the fabricated ASC device. (h) Cyclic retention of the device.

shape, indicating the good Coulombic efficiency of the ASC (rGO‖MnO$_2$–rGO) device. The obtained values of $C_{sp}$ (using eqn (S3), ESI†) are 216 F g$^{-1}$, 163 F g$^{-1}$, 160 F g$^{-1}$, 151 F g$^{-1}$, 118 F g$^{-1}$ and 104 F g$^{-1}$ at applied current densities of 1 A g$^{-1}$, 1.3 A g$^{-1}$, 1.6 A g$^{-1}$, 2 A g$^{-1}$, 2.5 A g$^{-1}$ and 3.5 A g$^{-1}$, respectively. The values of $C_{sp}$ at increasing current densities are gradually decreasing, as shown in Fig. 8(f). This shows that the ASC (rGO‖MnO$_2$–rGO) device retains good capacitance at higher current densities, implying the superior rate capability of the ASC device.[66] The GCD plots of the ASC device at varying cell potential and the calculated specific capacitance ($C_{sp}$) (using eqn (S3), ESI†) as the function of cell potential are depicted in Fig. S7(a) and (b) (ESI†), respectively. It should be noted that the value of $C_{sp}$ is gradually enhanced from 101 F g$^{-1}$ to 163 F g$^{-1}$ as the potential window rises from 1 V to 1.8 V, revealing the effectiveness of the fabricated ASC device with a wide potential window (as in our case here) in improving the capacitance in SCs. The Ragone plot (Fig. 8(g)) shows that the ASC device possesses the highest energy density of 24.25 W h kg$^{-1}$ along with a power density of 900 W kg$^{-1}$, and maintains it to 11.8 W h kg$^{-1}$ with a power density of 3000 W h kg$^{-1}$. Fig. 8(h) represents the capacity retention of the ASC device over 6000 GCD cycles at a current density of 5 A g$^{-1}$. It is observed that the device exhibited ∼90% retention over 6000 cycles.

Table 1 shows the comparative study of the electrochemical performance of the fabricated quasi solid-state sodium ion ASC (rGO‖MnO$_2$–rGO) device with recent literature reports based on

MnO$_2$–rGO as the positive electrode for the ASC device. Notably, the specific capacity, energy density and power capability of the ASC (rGO‖MnO$_2$–rGO) device are superior to other reported results due to the interconnected porous structure of the MnO$_2$ nano-needles and rGO sheets, which enhances the conductivity and provides a diffusion pathway for the intercalation and de-intercalation of the electrolyte ions. Additionally, the usage of the quasi solid-state sodium ion-based hydrogel membrane (PVA-Na$_2$SO$_4$) electrolyte plays a role in enhancing the ionic conductivity and electrode–electrolyte interface, and providing an increased cell potential of the device.

Fig. S7(c) (ESI†) shows the Nyquist plot of the ASC (rGO‖MnO$_2$–rGO) device before and after cycling in the frequency domain of 1 MHz to 1 mHz. The inset of Fig. S7(c) (ESI†) represents the equivalent circuit diagram. The obtained values of $R_s$ and $R_{ct}$ before and after cycling are reviewed in Table S2 (in ESI†). This indicates that the value of $R_{ct}$ is increased after cycling due to the continuous ion insertion/de-insertion, which damages the matrix, resulting in reduction of electrochemical sites and hence the capacitance decreases. Furthermore, to better understand the kinetics, the diffusion coefficient of the Na$^+$ ions was also extracted from the EIS spectra. The diffusion coefficient ($D$, cm$^2$ s$^{-1}$) was computed using eqn (S6) (ESI†). Fig. S6(d) (ESI†) depicts the curve of ($Z'$) *vs.* $\omega^{-0.5}$ for the ASC device before and after cycling at lower frequency. The calculated value of $D$ of Na$^+$ ions before and after cycling are mentioned in Table S2 (ESI†). The value of $D$ after the cycling

**Table 1** Comparison of this study with previous research reports based on the MnO$_2$–rGO-based positive electrode (cathode) for the asymmetric supercapacitor (ASC)

| S. No. | Anode material | Cathode material | Morphology of MnO$_2$ | Electrolyte | $C_{sp}$ (F g$^{-1}$) | Energy density (W h kg$^{-1}$) | Power density (W kg$^{-1}$) | Ref. |
|---|---|---|---|---|---|---|---|---|
| **1.** | **rGO** | **MnO$_2$–rGO** | **Nano-needle** | **PVA/Na$_2$SO$_4$** | **216 at 1 A g$^{-1}$** | **24.25** | **900** | **This work** |
| 2. | rGO | Fe$_2$O$_3$/MnO$_2$/rGO | Nanorod | PVA/KOH | 97 at 1 A g$^{-1}$ | 20.4 | 2099 | 34 |
| 3. | rGO | MnO$_2$ NF | Nano flower | 1 M Na$_2$SO$_4$ | 177.6 at 0.25 A g$^{-1}$ | 24.7 | 360.9 | 32 |
| 4. | rGO | MnO$_2$–rGO | Layer | PAAS/Na$_2$SO$_4$ | 27 F/g at 1 A g$^{-1}$ | 11.7 | 441 | 67 |
| 5. | AC | MnO$_2$–rGO | Nano-needle | 1 M Na$_2$SO$_4$ | 140 at 0.5 A g$^{-1}$ | 21 | 100 | 68 |
| 6. | Porous carbon | MnO$_2$–porous carbon | Nanowire | 1 M Na$_2$SO$_4$ | 24 at 0.2 A g$^{-1}$ | 20.8 | 250 | 33 |
| 7. | N-CNTs | N-CNTs/MnO$_2$ | Nanotube | 0.5 M Li$_2$SO$_4$ | 46.8 at 1 mA cm$^{-2}$ | 20.9 | 224 | 25 |
| 8. | N–P co doped carbon | MnO$_2$–N–P co doped carbon | Nanosheet | 1 M Na$_2$SO$_4$ | 71.58 at 0.5 A g$^{-1}$ | 32.21 | 449.8 | 69 |
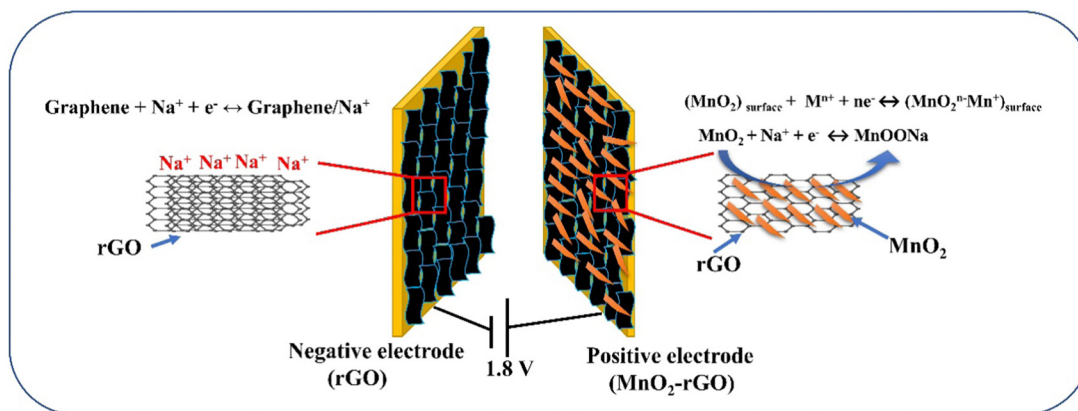


**Fig. 9** Charge storage mechanism of the wide 1.8 V voltage window quasi solid-state sodium ion ASC (rGO‖MnO$_2$–rGO) device.

reduces to $1.49 \times 10^{-10}$ from $2.15 \times 10^{-10}$ cm$^2$ s$^{-1}$. This reduction is ascribed to the distortion of the inter-connected porous structure of the MnO$_2$–rGO nanocomposite during the operation. Fig. S8 (ESI†) shows the fabricated actual ASC device with taking electrochemical results, and with lighting a 1.5 V bulb.

The charge storage kinetics of the ideal capacitive (EDLC)-type behavior of rGO and both capacitive and diffusive-like behavior of the MnO$_2$–rGO nanocomposite for the advanced 1.8 V quasi solid-state sodium ion ASC are depicted in Fig. 9. In the MnO$_2$–rGO nanocomposite (positive electrode), the synergistic effect of the interconnected MnO$_2$ nano-needles with the rGO sheets not only improves the pseudocapacitive contribution, but also enhances the conductivity of the MnO$_2$–rGO nanocomposite. This results in high capacitance and good cycle stability.[17] On the other hand, the rGO sheets make it possible for the ASC device to have a significant surface area and superior conductivity, which increases the capacitive contribution.[30] Therefore, the fabricated 1.8 V quasi solid-state ASC (rGO‖MnO$_2$–rGO) device shows a large specific capacitance, as well as high energy density and better performance, as compared to the recently reported ASCs with MnO$_2$–rGO as the positive electrode material.

## 5. Conclusion

In summary, a unique interconnected MnO$_2$ nanoneedles/rGO composite has been prepared by a simple hydrothermal route for utilization as the positive electrode material for an advanced sodium ion quasi-solid-state asymmetric supercapacitor (ASC). The electrochemical results in the three-electrode set-up reveal that rGO and the MnO$_2$–rGO nanocomposite possess good electrochemical performances when operated in negative and positive potential windows, respectively. The charge storage kinetic study of the electrodes is illustrated through the in-depth examinations of the CV profiles, which indicate the ideal capacitive nature of the rGO-electrode, and mixed capacitive and pseudocapacitive behavior of the MnO$_2$–rGO electrode. The assembled ASC (rGO‖MnO$_2$–rGO) device operated in the wide potential range of 0 V to 1.8 V yielded the highest specific capacitance of 216 F g$^{-1}$ at 1 A g$^{-1}$. Furthermore, the ASC (rGO‖MnO$_2$–rGO) device delivered the maximum energy density of 24.25 W h kg$^{-1}$ with a power density of 900 W kg$^{-1}$, along with a capacitance retention of ~90% over 6000 GCD cycles. The obtained performance of the ASC device is superior as compared to the previously reported work due to the interconnected hetero-structure of MnO$_2$–rGO, which not only prevents the restacking of the graphene sheet, but also provides the faster movement of ions during electrochemical processes. This study opens the gateway for the electrochemical study of the synthesized nano-structured composite material with different polymer electrolytes, and different morphologies of the composite can also be explored further for the other energy storage applications. Thus, this study delivers a new idea for developing morphological modified heterostructure composites, and a potential perspective for constructing quasi-solid-state devices for future energy storage systems.

## Author contributions

Deependra Jhankal: conceptualization, investigation, writing – original draft, methodology. Mohammed Saquib Khan: methodology, formal analysis, visualization. Preeti Shakya: formal analysis, data curation. Nikita Bhardwaj: formal analysis. Bhanu Yadav: data curation. K. K. Jhankal: investigation. K. Sachdev: formal analysis, validation, supervision.

## Conflicts of interest

There are no conflicts to declare.

## Acknowledgements

## References

1 W. Tuichai, A. Karaphun and C. Ruttanapun, *J. Alloys Compd.*, 2020, **849**, 156516.

2 V. Ruiz, R. Santamaría, M. Granda and C. Blanco, *Electrochim. Acta*, 2009, **54**, 4481–4486.

3 J. L. Yang, J. M. Cao, X. X. Zhao, K. Y. Zhang, S. H. Zheng, Z. Y. Gu and X. L. Wu, *Energy Chem.*, 2022, **4**, 100092.

4 A. Singh, S. K. Ojha, M. Singh and A. K. Ojha, *Electrochim. Acta*, 2020, **349**, 136349.

5 S. Ramesh, H. M. Yadav, K. Karuppasamy, D. Vikraman, H. S. Kim, J. H. Kim and H. S. Kim, *J. Mater. Res. Technol.*, 2019, **8**, 4227–4238.

6 Y. Ge, Z. Liu, Y. Wu and R. Holze, *Electrochim. Acta*, 2021, **366**, 137390.

7 T. Chen, F. Wang, S. Cao, Y. Bai, S. Zheng, W. Li, S. Zhang, S.-X. Hu and H. Pang, *Adv. Mater.*, 2022, **34**, 2201779.

8 M. Yu, Z. Wang, Y. Han, Y. Tong, X. Lu and S. Yang, *J. Mater. Chem. A*, 2016, **4**, 4634–4658.

9 J. Zhang, J. Jiang, H. Li and X. S. Zhao, *Energy Environ. Sci.*, 2011, **4**, 4009–4015.

10 C. H. Ng, H. N. Lim, S. Hayase, Z. Zainal, S. Shafie and N. M. Huang, *Electrochim. Acta*, 2017, **229**, 173–182.

11 Y. G. Wang, Z. D. Wang and Y. Y. Xia, *Electrochim. Acta*, 2005, **50**, 5641–5646.

12 H. Jiang, H. Niu, X. Yang, Z. Sun, F. Li, Q. Wang and F. Qu, *Chem. – Eur. J.*, 2018, **24**, 10683–10688.

13 S. Korkmaz, A. Kariper, O. Karaman and C. Karaman, *Ceram. Int.*, 2021, **47**, 34514–34520.

14 P. Yang, Y. Ding, Z. Lin, Z. Chen, Y. Li, P. Qiang, M. Ebrahimi, W. Mai, C. Ping Wong and Z. Lin Wang, *Nano Lett.*, 2014, **14**(2), 731–736.

15 Q. Liu, Z. Guo, C. Wang, S. Guo, Z. Xu, C. Hu, Y. Liu, Y. Wang, J. He and W. Y. Wong, *Adv. Sci.*, 2023, **10**, 1–13.

16 P. Ragupathy, H. N. Vasan and N. Munichandraiah, *J. Electrochem. Soc.*, 2008, **155**, A34.

17 Z. Ma, F. Jing, Y. Fan, L. Hou, L. Su, L. Fan and G. Shao, *Small*, 2019, **15**, 1–11.

18 J. Jiang and A. Kucernak, *Electrochim. Acta*, 2002, **47**, 2381–2386.

19 Q. Z. Zhang, D. Zhang, Z. C. Miao, X. L. Zhang and S. L. Chou, *Small*, 2018, **14**, 1–15.

20 R. Jiang, T. Huang, J. Liu, J. Zhuang and A. Yu, *Electrochim. Acta*, 2009, **54**, 3047–3052.

21 Y. Xiao, Y. Cao, Y. Gong, A. Zhang, J. Zhao, S. Fang, D. Jia and F. Li, *J. Power Sources*, 2014, **246**, 926–933.

22 E. Beaudrouet, A. Le Gal La Salle and D. Guyomard, *Electrochim. Acta*, 2009, **54**, 1240–1248.

23 K. Ghosh, C. Y. Yue, Md. M. Sk, R. K. Jena and S. Bi, *Sustainable Energy Fuels*, 2018, **2**, 280–293.

24 X. Zheng, P. Li, H. Zhu, K. Rui, G. Zhao, J. Shu, X. Xu, W. Sun and S. X. Dou, *Energy Storage Mater.*, 2018, **15**, 257–265.

25 J. Zhu, J. Hu, L. Wei, J. Liu and M. Zheng, *J. Power Sources*, 2018, **393**, 135–144.

26 J. Ju, H. Zhao, W. Kang, N. Tian, N. Deng and B. Cheng, *Electrochim. Acta*, 2017, **258**, 116–123.

27 R. K. Sharma, A. C. Rastogi and S. B. Desu, *Electrochim. Acta*, 2008, **53**, 7690–7695.

28 C. Liu, Y. Bai, W. Li, F. Yang, G. Zhang and H. Pang, *Angew. Chem., Int. Ed.*, 2022, **61**, e202116282.

29 Y. Huang, H. Cheng, D. Shu, J. Zhong, X. Song, Z. Guo, A. Gao, J. Hao, C. He and F. Yi, *Chem. Eng. J.*, 2017, **320**, 634–643.

30 Y. Xie, C. Yang, P. Chen, D. Yuan and K. Guo, *J. Power Sources*, 2019, **425**, 1–9.

31 M. S. Khan, D. Jhankal, P. Shakya, A. K. Sharma, M. K. Banerjee and K. Sachdev, *Carbon*, 2023, **208**, 227–237.

32 G. A. M. Ali, *J. Electron. Mater.*, 2020, **49**, 5411–5421.

33 L. Li, S. Pang, X. Fan, Y. Wang, H. Cheng, D. Fang, L. Qin, M. Deng and Z. Lu, *Mater. Technol.*, 2021, 1–9.

34 M. Geerthana, S. Prabhu and R. Ramesh, *J. Energy Storage*, 2022, **47**, 103529.

35 D. J. Tarimo, K. O. Oyedotun, A. A. Mirghni, N. F. Sylla and N. Manyala, *Electrochim. Acta*, 2020, **353**, 136498.

36 B. Zhao, P. Liu, Y. Jiang, D. Pan, H. Tao, J. Song, T. Fang and W. Xu, *J. Power Sources*, 2012, **198**, 423–427.

37 L. Zhang, H. Liu, H. Ruan, Y. Su, R. Hu, L. Tian, Z. Hu and J. Li, *Int. J. Electrochem. Sci.*, 2016, **11**, 10815–10826.

38 A. Ogata, S. Komaba, R. Baddour-Hadjean, J. P. Pereira-Ramos and N. Kumagai, *Electrochim. Acta*, 2008, **53**, 3084–3093.

39 C. Gomez-Navarro, R. T. Weitz, A. M. Bittner, M. Scolari, A. Mews, M. Burghard and K. Kern, *Nano Lett.*, 2009, **9**, 2206.

40 S. Ghasemi, S. R. Hosseini and O. Boore-talari, *Ultrason. Sonochem.*, 2018, **40**, 675–685.

41 M. Xu, L. Kong, W. Zhou and H. Li, *J. Phys. Chem. C*, 2007, **111**, 19141–19147.

42 N. Sharma, V. Sharma, S. K. Sharma and K. Sachdev, *Mater. Lett.*, 2019, **236**, 444–447.

43 M. Choi, S. Kumar, D. Yoon, J. Hwang, S. Min and J. Kim, *J. Power Sources*, 2016, **309**, 202–211.

44 V. Sannasi and K. Subbian, *J. Mater. Sci.: Mater. Electron.*, 2020, **31**, 17120–17132.

45 G. Qin, H. Zhang, H. Liao, Z. Li, J. Tian, Y. Lin, D. Zhang and Q. Wu, *J. Mater. Sci.*, 2017, **52**, 10981–10992.

46 J. Zhang, Y. Xu, Z. Liu, W. Yang and J. Liu, *RSC Adv.*, 2015, **5**, 54275–54282.

47 K. H. Ye, Z. Q. Liu, C. W. Xu, N. Li, Y. B. Chen and Y. Z. Su, *Inorg. Chem. Commun.*, 2013, **30**, 1–4.

48 Z. Li, Y. Mi, X. Liu, S. Liu, S. Yang and J. Wang, *J. Mater. Chem.*, 2011, **21**, 14706–14711.

49 D. Guo, S. Dou, X. Li, J. Xu, S. Wang, L. Lai, H. K. Liu, J. Ma and S. X. Dou, *Int. J. Hydrogen Energy*, 2016, **41**, 5260–5268.

50 D. P. Dubal, A. D. Jagadale, S. V. Patil and C. D. Lokhande, *Mater. Res. Bull.*, 2012, **47**, 1239–1245.

51 M. Saraf, K. Natarajan and S. M. Mobin, *ACS Appl. Mater. Interfaces*, 2018, **10**, 16588–16595.

52 J. Wang, J. Polleux, J. Lim and B. Dunn, *J. Phys. Chem. C*, 2007, **111**, 14925–14931.

53 N. Kanaujiya, N. Kumar, M. Singh, Y. Sharma and G. D. Varma, *J. Energy Storage*, 2021, **35**, 102302.

54 J. Pati, H. Raj, S. K. Sapra, A. Dhaka, A. K. Bera, S. M. Yusuf and R. S. Dhaka, *J. Mater. Chem. A.*, 2022, **10**, 15460–15473.

55 T. Brezesinski, J. Wang, S. H. Tolbert and B. Dunn, *Nat. Mater.*, 2010, **9**, 146–151.

56 N. Choudhary, C. Li, J. Moore, N. Nagaiah, L. Zhai, Y. Jung and J. Thomas, *Adv. Mater.*, 2017, 1605336.

57 R. Thangappan, S. Kalaiselvam, A. Elayaperumal, R. Jayavel, M. Arivanandhan, R. Karthikeyan and Y. Hayakawa, *Dalton Trans.*, 2016, **45**, 2637–2646.

58 S.-L. Kuo and N.-L. Wu, *J. Electrochem. Soc.*, 2006, **153**, A1317.

59 M. Toupin, T. Brousse and D. Bélanger, *Chem. Mater.*, 2004, **16**, 3184–3190.

60 D. Guo, X. Chen, Z. Fang, Y. He, C. Zheng, Z. Yang, K. Yang, Y. Chen and S. Huang, *Electrochim. Acta*, 2015, **176**, 207–214.

61 D. Jhankal, M. S. Khan, B. Yadav, P. Shakya, N. Bhardwaj, K. K. Jhankal and K. Sachdev, *Energy Storage*, 2023, 1–11.

62 S. Liang, H. Wang, Y. Li, H. Qin, Z. Luo and L. Chen, *Appl. Surf. Sci.*, 2021, **567**, 150809.

63 J. Ye, B. Hu, Y. Jin, Z. Wang, Y. Xi, L. Fang and Q. Pan, *Electrochim. Acta*, 2020, **349**, 136372.

64 S. Rani, N. Kumar, A. Tandon and Y. Sharma, *IEEE Trans. Electron Devices*, 2021, **68**, 251–256.

65 N. Kurra, S. Uzun, G. Valurouthu and Y. Gogotsi, *Energy Storage Mater.*, 2021, **39**, 347–353.

66 P. Makkar and N. N. Ghosh, *Ind. Eng. Chem. Res.*, 2021, **60**(4), 1666–1674.

67 H. Fei, N. Saha, N. Kazantseva, R. Moucka and Q. Cheng, *Materials*, 2017, **10**, 1251.

68 E. Miniach, A. Śliwak, A. Moyseowicz, L. Fernández-Garcia, Z. González, M. Granda, R. Menendez and G. Gryglewicz, *Electrochim. Acta*, 2017, **240**, 53–62.

69 P. Wu, M. Gao, S. Yu, M. Feng, S. Liu and J. Fu, *Electrochim. Acta*, 2020, **354**, 136681.